



# Infrared Dark Clouds and High-mass Star Formation Activity in Galactic Molecular Clouds

R. Retes-Romero<sup>1</sup> , Y. D. Mayya , A. Luna, and L. Carrasco

Instituto Nacional de Astrofísica, Óptica y Electrónica, Luis Enrique Erro 1, Tonantzintla, Puebla, C.P. 72840, México; rretes@inaoep.mx, ydm@inaoep.mx, aluna@inaoep.mx, carrasco@inaoep.mx

Received 2019 July 23; revised 2020 May 12; accepted 2020 May 12; published 2020 July 1

## Abstract

Ever since their discovery, infrared dark clouds (IRDCs) are generally considered to be the sites just at the onset of high-mass (HM) star formation. In recent years, it has been realized that not all IRDCs harbor HM young stellar objects (YSOs). Only those IRDCs satisfying a certain mass–size criterion, or equivalently above a certain threshold density, are found to contain HMYSOs. In all cases, IRDCs provide ideal conditions for the formation of stellar clusters. In this paper, we study the massive stellar content of IRDCs to readdress the relation between IRDCs and HM star formation. For this purpose, we have identified all IRDCs associated with a sample of 12 Galactic molecular clouds (MCs). The selected MCs have been the target of a systematic search for YSOs in an earlier study. The cataloged positions of YSOs have been used to search all YSOs embedded in each identified IRDC. In total, we have found 834 YSOs in 128 IRDCs. The sample of IRDCs have mean surface densities of  $319 M_{\odot} \text{ pc}^{-2}$ , mean mass of  $1062 M_{\odot}$ , and a mass function power-law slope  $-1.8$ , which are similar to the corresponding properties for the full sample of IRDCs and resulting physical properties in previous studies. We find that all those IRDCs containing at least one intermediate to HM young star satisfy the often-used mass–size criterion for forming HM stars. However, not all IRDCs satisfying the mass–size criterion contain HM stars. We find that the often-used mass–size criterion corresponds to 35% probability of an IRDC forming a massive star. Twenty-five (20%) of the IRDCs are potential sites of stellar clusters of mass more than  $100 M_{\odot}$ .

*Unified Astronomy Thesaurus concepts:* Interstellar medium (847); Infrared dark clouds (787); Star formation (1569); Young stellar objects (1834); Protostars (1302); Protoclusters (1297)

*Supporting material:* machine-readable tables

## 1. Introduction

Infrared dark clouds (IRDCs) are dark silhouettes observed in the mid-infrared (MIR) due to the contrast of the absorption against the bright emission of the Galactic background in the MIR images first observed using the Infrared Space Observatory survey (Perault et al. 1996) and the Midcourse Space Experiment (Egan et al. 1998). These regions are associated with the densest regions of the Galactic molecular clouds (MCs) and have physical conditions such as low temperatures ( $T < 25$  K) and high densities ( $n \gtrsim 10^5 \text{ cm}^{-3}$ ) (Rathborne et al. 2009; Ragan et al. 2013). These conditions compare well with those present in high-mass star-forming (HMSF) regions (Rathborne et al. 2006; Simon et al. 2006; Beuther & Steinacker 2007). Follow-up studies confirm IRDCs as birthplaces of high-mass (HM) stars and possibly stellar clusters as well (Kauffmann & Pillai 2010; Henshaw et al. 2014; Wang et al. 2014). Thus, IRDCs offer an opportunity to understand the details of HMSF process, and particularly, the stellar cluster formation.

Stars form in compact subparsec-sized cores usually embedded at the densest parts of the IRDCs. Results of Alves et al. (2007) and André et al. (2010) show that the form of the core mass function resembles well the initial mass function (IMF) of stars. This suggests that the process driving the fragmentation of the progenitor cloud into cores principally establishes the form of the stellar IMF. Given their compactness, cores can be detected only in nearby MCs. The densest

structures seen in emission in farther MCs have sizes of  $\sim 1$  pc, and are often referred to as clumps. These clumps have mass function that resembles the mass function of giant MCs with an index ranging from 1.8 Kramer et al. (1998) to 2.1 Simon et al. (2001).

The similarity in physical properties (size, density, mass, etc.) of IRDCs and the clumps (Rathborne et al. 2006; Ragan et al. 2013), makes the study the IRDC mass distribution of great importance. Studies so far have not found any noticeable differences in the power-law ( $\frac{dN}{dM} \propto M^{\alpha}$ ) indices for the IRDCs and the clumps with  $\alpha$  clustered around  $-2.0$ . The results of some of these studies are summarized here. Rathborne et al. (2006) reported  $\alpha = -2.1$  for clumps embedded in IRDCs, whereas Simon et al. (2006) using observations in  $^{13}\text{CO}$  emission for an IRDCs sample, found  $\alpha = -1.97$ . Ragan et al. (2009) reported a broken power law, with  $\alpha = -1.76$  for masses greater than  $40 M_{\odot}$ . Peretto & Fuller (2010) (hereafter PF10) reported  $\alpha = -1.85$  for masses greater than  $100 M_{\odot}$  for IRDCs. Recently, Gomez Gonzalez (2012) using observations at 1.2 mm, reported  $\alpha = -1.6$  in the mass range from  $15 M_{\odot}$  to  $3000 M_{\odot}$ , for massive clumps.

Theoretical studies have shown that the HMSF can occur only in regions that have gas densities above the threshold densities of  $1 \text{ g cm}^{-3}$  ( $4790 M_{\odot} \text{ pc}^{-2}$ ) (Krumholz & McKee 2008). Rathborne et al. (2009) found that the surface gas densities in IRDCs are often above this threshold. Kauffmann et al. (2010) defined an empirical mass–size threshold relation to identify clouds that may contain HM star formation sites, by studying Galactic MCs with and without HM star formation. Kauffmann & Pillai (2010) found that  $\sim 25\%$ – $50\%$  of the

<sup>1</sup> Current address: Decanato de Ingeniería, UPAEP, 21 Sur 1103, Barrio de Santiago, C.P. 72410, Puebla, México.

**Table 1**  
Summary of the Properties of the M Sample where IRDCs have been Searched

GM	IRAS name	Lon (deg)	Lat (deg)	$D$ (kpc)	$M_{\text{LTE}}$ ( $M_{\odot}$ )	$N(\text{YSOs})$	$N(\text{IRDCs})$	$\Sigma_{\text{gas}}$ ( $M_{\odot} \text{ pc}^{-2}$ )	$\Sigma_{\text{SFR}}$ ( $M_{\odot} \text{ Myr}^{-1} \text{ pc}^{-2}$ )	SFE (%)
(1)	(2)	(3)	(4)	(5)	(6)	(7)	(8)	(9)	(10)	(11)
MC1	19230 + 1506	50.28	-0.39	1.3 (0.2)	0.33 (0.17)	130	6	210 (114)	3.3 (1.7)	2.7 (0.3)
MC2	19236 + 1456	50.22	-0.61	3.4 (0.4)	3.07 (1.55)	556	23	155 (79)	2.1 (1.1)	2.2 (0.1)
MC9	19139 + 1113	45.82	-0.28	4.8 (0.6)	2.56 (1.10)	861	9	646 (332)	19.1 (9.6)	3.9 (0.2)
MC12	19132 + 1035	45.19	-0.44	5.4 (0.6)	2.24 (1.12)	170	3	358 (179)	1.1 (0.6)	0.5 (0.1)
MC20	19074 + 0814	42.43	-0.26	4.9 (0.6)	2.44 (1.20)	292	5	647 (320)	6.4 (3.3)	1.2 (0.1)
MC21	19074 + 0752	42.11	-0.44	3.9 (0.5)	3.52 (1.59)	672	15	133 (60)	2.3 (1.2)	2.6 (0.2)
MC23	19048 + 0748	41.75	0.09	1.0 (0.1)	0.30 (0.22)	592	1	320 (240)	26.8 (13.5)	11.9 (0.7)
MC75	18232-1154	19.49	0.15	2.3 (0.3)	2.32 (1.20)	596	7	613 (320)	5.6 (2.8)	1.5 (0.1)
MC76	18236-1205	19.36	-0.02	2.5 (0.3)	3.14 (1.74)	666	25	565 (310)	7.5 (3.7)	2.1 (0.1)
MC78	18223-1243	18.66	-0.06	3.7 (0.4)	13.52 (6.46)	721	25	763 (365)	4.6 (2.3)	0.8 (0.1)
MC80	18205-1316	17.96	0.08	2.2 (0.3)	9.57 (5.03)	661	7	816 (410)	5.6 (2.8)	1.2 (0.1)
MC81	18190-1414	16.94	-0.07	2.1 (0.3)	0.23 (0.11)	14	3	218 (64)	1.0 (0.7)	0.8 (0.3)

**Note.** Columns: (1) Name of the MC; (2) Name of the principal IRAS source in the MC; (3–4) Galactic longitude and latitude in degree; (5) Kinematical distance (with an error of 12%) to the dense clump associated with the IRAS source from Faúndez et al. (2004); (6) Mass of the M obtained using the LTE method; (7–8) Number of YSOs and IRDCs spatially associated with the MC; (9) Surface gas density of the MC; (10) Surface density of star formation rate of the MC; and (11) Star formation efficiency in % units in each cloud.

(This table is available in machine-readable form.)

IRDCs in the samples from Rathborne et al. (2006) and Peretto & Fuller (2009) belong to clouds that are above the mass–size threshold relation. Star-forming (SF) clumps from Bolocam Survey also obey the threshold relation (Svoboda et al. 2016). Thus, there is overwhelming support for the idea that IRDCs are potential HMSF sites.

In a recent work, we (Retes-Romero et al. 2017, hereafter R17) studied the young stellar Object (YSO) populations in a sample of 12 Galactic MCs. Each chosen M contains a CS clump associated with young luminous IRAS sources, as well as the presence of HMSF tracers such as a methanol,  $\text{H}_2\text{O}$  and OH maser emitting sources and SiO outflows. The line of sight to each M is devoid of any intervening MC as inferred from their  $^{13}\text{CO}$  profiles. We used the Galactic rotation curve model of Clemens (1985) to infer the kinematical distances to all our sample MCs, assigning in all cases the near distance, when there is distance ambiguity. The IRDCs cataloged in the present work are embedded in the MCs, hence the M distances also apply to the IRDCs. It is important to note that this association of our sample IRDCs to MCs eliminates the usual problem of determining distances to IRDCs. Hence, our distances to IRDCs only suffer from the error involved in the kinematical distance method, which is estimated to be 12% by Faúndez et al. (2004). This distance error is comparable with the 15% accuracy quoted by Simon et al. (2001) for MCs from the Milky Way Galactic Ring Survey (GRS) using  $^{13}\text{CO}$  data. However, the error in the distance can be much greater than the 12%–15% mentioned here and vary depending on longitude and near/far side, as found by Roman-Duval et al. (2009). The introduction of the error on distance is the main source of uncertainty on the physical parameters of the IRDCs.

In addition, stellar masses are available for all embedded YSOs. All these characteristics of our data set offer us an opportunity to study quantitatively the HM star formation, as well as stellar cluster formation in IRDCs of wide ranging masses and sizes. The data set also allows, for the first time, an exploration of whether a star formation rate–surface density relation, commonly referred to as the Kennicutt–Schmidt (K–S)

law (Kennicutt 1998), is applicable within the IRDCs. It may be noted that, K–S law though primarily applicable on kiloparsec scales in extragalactic objects with a power-law index of 1.4, is also applicable within individual Galactic MCs. Willis et al. (2015) found the index to be varying between 1.77 and 2.86 for HMSF regions, whereas for our sample of 12 MCs, index is found to vary between 1.4 and 3.6.

The structure of the paper is the following. In Section 2, we describe our sample of IRDCs. Their mass and size distributions are given in Section 3. The SF properties in our sample of IRDCs are discussed in Section 4. We summarize our conclusions in Section 5.

## 2. IRDC Sample and Analysis

The sample of IRDCs in the present study consists of all those associated with the 12 MCs studied by R17, and are drawn from the Peretto & Fuller (2009) IRDC catalog (hereafter PF09). All MCs in this sample have at least one HMSF site, as characterized by a dense clump detected in CS( $J=2-1$ ) line emission and 1.2 mm dust continuum millimeter emission (Bronfman et al. 1996; Faúndez et al. 2004), associated with maser emitting toward to IRAS sources. The MCs were defined using the  $^{13}\text{CO}$  ( $J=1-0$ ) line emission data from the GRS (Jackson et al. 2006). All of the molecular gas that is above a column density of gas equivalent to  $A_v = 1$  mag and is within  $5 \text{ km s}^{-1}$  of the CS peak velocity is considered to be part of the MC. In Table 1, we give the physical properties of these MCs. Our MCs are at distances (kinematical) of 1–5.4 kpc, have masses (LTE method) in the range  $(2.3-135) \times 10^3 M_{\odot}$ , and  $\Sigma_{\text{SFR}} = 1-27 M_{\odot} \text{ Myr}^{-1} \text{ pc}^{-2}$  (Retes-Romero et al. 2017).

### 2.1. Selection of IRDCs Associated with the MCs

The PF09 catalog is the most complete source of IRDCs seen on Spitzer  $8 \mu\text{m}$  images. PF09 defined an IRDC as a connected structure with a threshold opacity in Spitzer  $8 \mu\text{m}$  band ( $\tau_8$ ) of  $0.35$  ( $N_{\text{H}_2} = 2 \times 10^{21} \text{ cm}^{-2}$ ) and an angular size greater than  $4''$ . A visual inspection of our cloud locations on the  $8 \mu\text{m}$

**Table 2**  
Observed and Derivated Parameters of Individual IRDCs

ID	Lon (deg)	Lat (deg)	$a$ (arcsec)	$b$ (arcsec)	$\theta$ (deg)	$\tau_8$	Area (pc <sup>2</sup> )	$R_{\text{eff}}$ (pc)	$M$ ( $M_{\odot}$ )	$\Sigma$ ( $M_{\odot} \text{ pc}^{-2}$ )	$\Sigma_{\text{SFR}}$ ( $M_{\odot} \text{ Myr}^{-1} \text{ pc}^{-2}$ )
(1)	(2)	(3)	(4)	(5)	(6)	(7)	(8)	(9)	(10)	(11)	(12)
MC78-IRDC1	18.6810	−0.0510	87.1	23.8	20	0.60	2.07(0.52)	0.81(0.06)	794(88)	383(42)	1.69(0.66)
MC78-IRDC2	18.6240	−0.0700	361.5	70.3	−22	0.71	25.39(6.35)	2.84(0.20)	11514(1267)	453(50)	1.40(0.55)
MC78-IRDC3	18.6890	−0.0930	55.5	24.9	23	0.51	1.38(0.35)	0.66(0.05)	450(50)	326(36)	0.18(0.07)
MC78-IRDC4	18.6410	−0.1140	12.0	5.9	52	0.42	0.07(0.02)	0.15(0.01)	19(3)	268(30)	3.52(1.38)
MC78-IRDC5	18.7020	−0.1000	25.5	19.3	60	0.46	0.49(0.12)	0.39(0.03)	144(16)	294(32)	0.49(0.19)
MC78-IRDC6	18.6970	0.0030	28.5	26.0	−35	0.46	0.74(0.19)	0.48(0.03)	218(24)	294(32)	0.32(0.13)
MC78-IRDC7	18.6320	−0.1360	27.7	5.3	75	0.45	0.15(0.04)	0.21(0.02)	42(5)	287(32)	1.64(0.64)
MC78-IRDC8	18.7460	−0.0120	32.9	14.9	67	0.58	0.49(0.12)	0.39(0.03)	181(20)	370(41)	0.49(0.19)
MC78-IRDC9	18.7620	−0.0290	66.9	18.7	46	0.57	1.25(0.31)	0.63(0.04)	455(51)	364(40)	0.60(0.23)
MC78-IRDC10	18.7900	−0.0250	30.5	20.9	26	0.70	0.64(0.16)	0.45(0.03)	285(32)	447(49)	5.10(1.98)
...	...	...	...	...	...	...	...	...	...	...	...

**Note.** Columns: (1) ID of the IRDC; (2–3) Galactic coordinates of the IRDC centroid; (4–5) major ( $a$ ) and minor ( $b$ ) axes of the ellipse that best matches the IRDC; (6) orientation angle of the ellipse; (7) (mean) opacity in the Spitzer 8  $\mu\text{m}$  band; (8) area of the IRDC; (9) Effective radius of the IRDC; (10) Mass of the IRDC; (11) Surface gas density, and (12) Surface density of the star formation rate of the IRDC. The data for columns 2–7 are taken of PF09 catalog, and columns 8–12 are derived in this work.

(This table is available in its entirety in machine-readable form.)

Spitzer images shows IRDCs. We selected all IRDCs from the PF09 catalog that are within the boundaries of our MCs, defined previously using a columnar gas threshold. In the 8  $\mu\text{m}$  images of the SF regions of our sample, intense emission and absorption zones coexist spatially. This hinders the identification of structures such as the IRDCs. Thus, we performed a visual inspection for spatial association of the positions of IRDCs and dark patches in the 8  $\mu\text{m}$  images. The IRDCs without spatial association were rejected from the sample. Column 8 of Table 1 gives the number of IRDCs associated with each MC. The complete IRDC sample contains 128 objects; their names, coordinates, and observed/derived parameters are listed in Table 2. The printed version contains 10 sources to guide the reader and the complete table is given in the electronic version. The positions of IRDCs most often coincide with the densest <sup>13</sup>CO contours of the MCs. This is illustrated for the IRAS 18223-1243 (MC78) region in Figure 1. IRDCs with major axis sizes larger than the <sup>13</sup>CO beam size of 46'' are clearly associated with the densest contours of the MCs.

### 3. Physical Properties of the IRDCs Associated with the MCs

To obtain the masses of the IRDCs, we obtained the surface gas density ( $\Sigma_{\text{gas}}$ ) and physical area of each object. These parameters are obtained using the mean opacity ( $\tau_8$ ) in the Spitzer 8  $\mu\text{m}$  band and the apparent size of the IRDCs, taken from the PF09 catalog. To compute the surface gas density of each IRDC, we used the expression (Butler & Tan 2012),

$$\left[ \frac{\Sigma_{\text{gas}}}{M_{\odot} \text{ pc}^{-2}} \right] = 622.7 \times \tau_8, \quad (1)$$

where a gas-to-dust ratio of 156 (Ossenkopft & Henning 1994; Butler & Tan 2012), and an equivalence  $1 \text{ g cm}^{-3} = 4790 M_{\odot} \text{ pc}^{-2}$  have been used, assuming a 1 pc depth.

The  $\Sigma_{\text{gas}}$  distribution for our sample of IRDCs is shown in Figure 2, along with that for the full PF09 sample. The mean value of  $319 M_{\odot} \text{ pc}^{-2}$  ( $\sim 0.07 \text{ g cm}^{-2}$ ) for our sample compares very well with the mean value for the PF09 sample of

$\Sigma_{\text{gas}} = 320 M_{\odot} \text{ pc}^{-2}$ . The distributions also have very similar ranges. This illustrates that our sample of IRDCs is representative of the full sample of IRDCs in PF09. The properties of our sample are also similar to that reported for Galactic dense clumps with or without star formation (Ragan et al. 2013; Schisano et al. 2014). Figure 2 shows that there is a small range in gas-surface densities ( $\Sigma_{\text{gas}} \sim 250\text{--}500 M_{\odot} \text{ pc}^{-2}$ ) that likely arises from an observational limitation. IRDCs are selected in absorption against the galactic background light at  $\sim 8 \mu\text{m}$ . This technique is sensitive only for a small range of gas densities, as shown in the Figure 2 for the complete IRDC sample of PF09. At low densities, the absorption is not strong enough to be detected, whereas at high densities, the cloud becomes optically thick at 8  $\mu\text{m}$ . The technique underestimates the opacity when the region contains an 8  $\mu\text{m}$  emitting source. When the cloud starts forming stars, such sources are expected, hence the true gas-surface densities for SF clouds are likely to be higher than that inferred from  $\tau_8$ . Given that we use the mean value of  $\tau_8$  from each IRDC to obtain its  $\Sigma_{\text{gas}}$  value, an agglomeration of  $\Sigma_{\text{gas}}$  values in a narrow dynamic range is expected, as observed in Figures 2 and 9.

The masses of the IRDCs are obtained using the expression,  $M = \text{area} \times \Sigma_{\text{gas}}$ , where the area is the area of the ellipse associated with each IRDC (see the definition in PF09) and obtained from the major and minor axis angular sizes (see Table 2) and distance to the M containing each IRDC (Table 1). The effective radius ( $R_{\text{eff}}$ ) is obtained assuming a circular symmetry and using the expression,  $R_{\text{eff}} = \sqrt{\text{area}/\pi}$ . We use this  $R_{\text{eff}}$  as a size indicator in the analysis of mass–size distribution. The values of  $\Sigma_{\text{gas}}$ , area,  $R_{\text{eff}}$ , and other derived parameters of the clouds are listed in Table 2. The uncertainties in the derived parameters are obtained by propagating the distance errors.

However, uncertainty in  $\tau_8$  can originate from several factors (which are considered beyond the scope of this work). (a) The selection of the MIR opacity model pointed out by Butler & Tan (2012). The variation of opacity per unit gas mass, which is dependent on the model used, gives an uncertainty value of up to 30% in the  $\tau_8$ , but in IRDCs typically is already 20%. (b) The variation on the background intensity, which can lead to

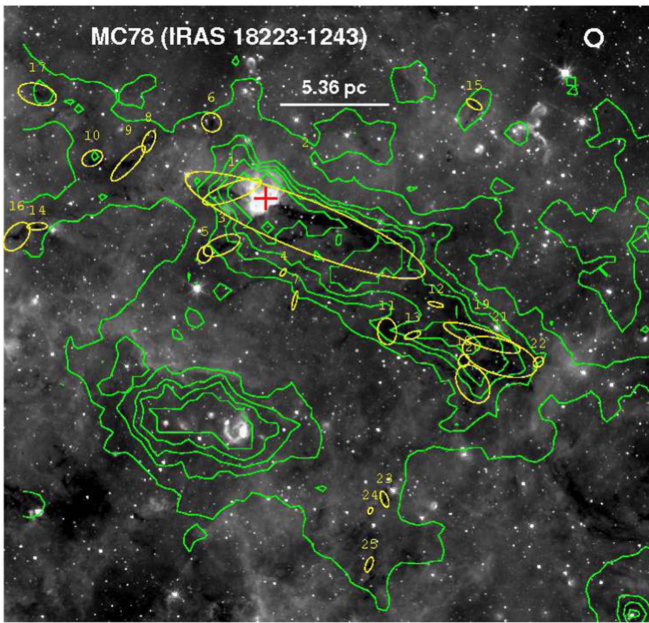


**Figure 1.** Illustration of the locations of our sample of IRDCs (numbered yellow ellipses) on the Spitzer 8  $\mu\text{m}$  band image (grayscale) for one of our sample MCs (IRAS 18223-1243; MC78). The  $^{13}\text{CO}$  emission is shown as green contours, starting at  $N_{\text{H}_2} = 10^{21} \text{ cm}^{-2}$ , and increasing in linear steps of  $5.0 \times 10^{21} \text{ cm}^{-2}$ . The MC78 is associated with the protostellar source IRAS 18223-1243, whose location is indicated by a red cross. The physical scale of 5.36 pc is equivalent to  $5'$  angular scale. The  $^{13}\text{CO}$  beam (white circle) is shown at the top right corner.

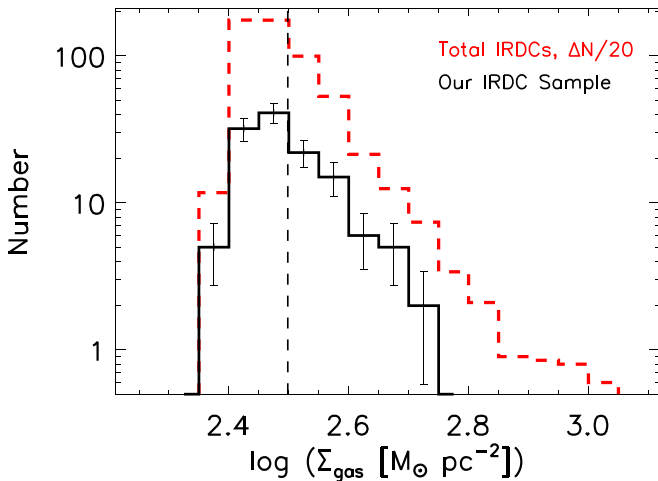


**Figure 2.** Distribution of gas-surface density for our sample of IRDCs (black solid histogram) compared with that for the full IRDC sample of PF09 (red dashed histogram; after scaling down the numbers by a factor of 20). The error bars for our sample correspond to the statistical uncertainties in each bin ( $\sqrt{N}$ ). The vertical dashed line indicates the mean value ( $319 M_{\odot} \text{ pc}^{-2}$ ) for our sample, which agrees very well with the mean value for the PF09 sample.

flux uncertainties of 10% ( $\Sigma_{\text{gas}} \sim 0.01 \text{ g cm}^{-2}$ , for Galactic diffuse MIR emission; Butler & Tan 2012). Another source of uncertainty is caused by foreground MIR emission along our line of sight to the IRDC. The effect is minimized by choosing IRDCs that are relatively nearby, which is the case for the IRDCs in the R17 M sample.

The distribution of the mass and area of our IRDCs is shown in Figure 3. The vertical dotted lines at  $2 M_{\odot}$  and  $50 M_{\odot}$  indicate the limit of detection in mass, which is obtained using

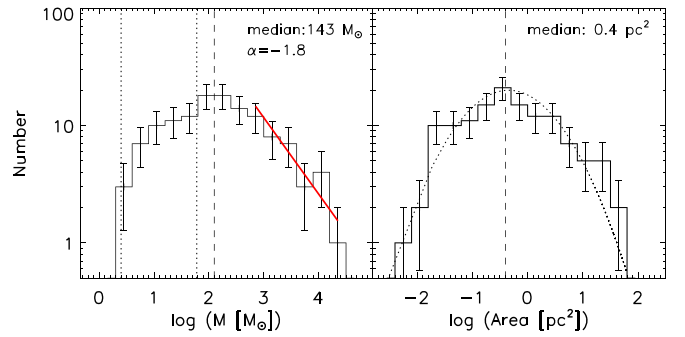


**Figure 3.** Mass (left) and area (right) distribution of the IRDCs. The median value of the mass distribution ( $143 M_{\odot}$ ) is shown by the vertical dashed line. The range of mass for the limit of detection of IRDCs in the PF10 catalog is marked by the dotted vertical lines at  $2 M_{\odot}$  and  $50 M_{\odot}$ . The observed distribution for higher values of mass than this range is in agreement with a power-law fit (red solid line) with an index  $\sim -1.8$ . (Right) The area histogram is well represented by a log normal function (dashed line). The error bars correspond to the statistical uncertainties in each bin ( $\sqrt{N}$ ) in both histograms.

the definition of an IRDC in the Spitzer 8  $\mu\text{m}$  data (PF10) for a distance range from 1 to 5.4 kpc, corresponding to our IRDC sample. For masses above this mass range, the distribution follows a power-law functional form given by

$$\frac{dN}{dM} \propto M^{\alpha}, \quad (2)$$

where  $M$  is the mass of the IRDC, and  $N$  is the number of the IRDCs in each mass bin. A linear regression (weighted by errors) in this regime gives  $\alpha \sim -1.8$ . This index is consistent with the resulting index of  $-1.85$  of Peretto & Fuller (2010) for IRDCs, and the values  $-2.1$ ,  $-1.97$ , and  $-1.76$  reported by Rathborne et al. (2006), Simon et al. (2006), and Ragan et al. (2009), respectively, for clump mass distributions in IRDCs. It may be noted that a power law functions with similar index values are also found for the prestellar and protostellar mass distributions (André et al. 2010; Könyves et al. 2010) and for stellar masses in young star clusters (see the review of Bastian et al. 2010, their Section 2.3.2).

To determine the surface density of the star formation rate ( $\Sigma_{\text{SFR}}$ ) in the IRDCs, we obtained the spatial association of the YSOs within the ellipse defined for each IRDC. The positions and masses of the YSOs are taken from R17.

The method for obtaining the stellar masses and  $\Sigma_{\text{SFR}}$  is fully detailed in R17 and briefly explained below. As a first step, we determined the bolometric luminosity of each YSO, using a class-dependent conversion factor from the 24  $\mu\text{m}$  luminosity to bolometric luminosity. We used Spitzer MIR photometry data set for determining the spectral energy distribution evolutionary phase (Class I, II, and III) and the 24  $\mu\text{m}$  fluxes. We used the pre-main-sequence evolutionary tracks of Tognelli et al. (2011) to relate bolometric luminosities to stellar masses. We added masses of all YSOs within the ellipse defined in columns 4, 5, and 6 of Table 2 to determine the total stellar mass associated with each IRDC. We then divided this total mass by the area of the ellipse and the typical timescale that stars spend in each evolutionary class from Hartmann & Kenyon (1996) and Evans et al. (2009) to obtain  $\Sigma_{\text{SFR}}$ . For IRDCs without associated YSOs, we assigned a minimum stellar mass corresponding to one YSO of mass  $0.5 M_{\odot}$  to obtain a lower limit value of  $\Sigma_{\text{SFR}}$ . The  $\Sigma_{\text{SFR}}$  values are shown in column 12 of Table 2.

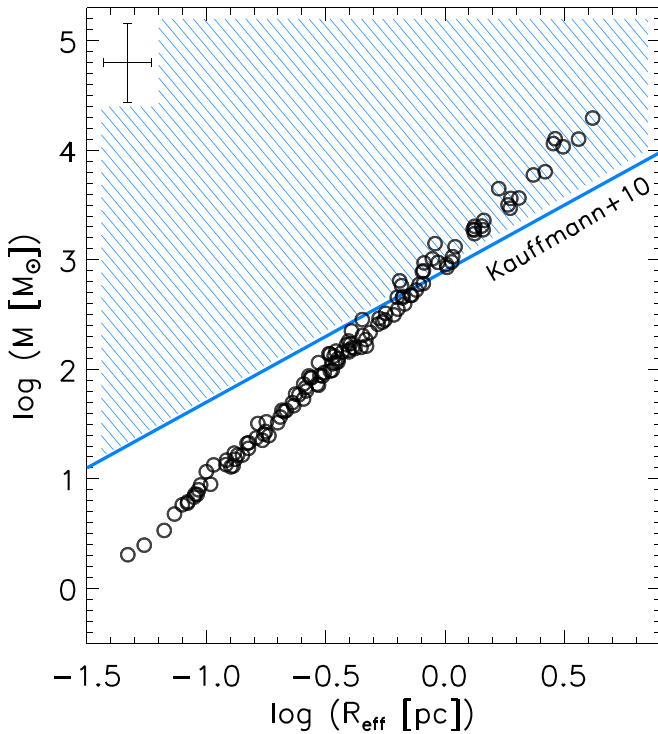


**Figure 4.** Mass–size diagram for the sample IRDCs, using  $R_{\text{eff}}$  (black circles) as a proxy for size. The striped area shows the parameter space where IRDCs are expected to harbor HM star progenitors following the criterion of Kauffmann et al. (2010, diagonal solid line). The mean error of the data is shown in the upper left region of the diagram.

## 4. Analysis and Discussion

### 4.1. The IRDCs as Birthplaces of High-mass Stars

The HM star formation process requires a HM concentration in a relatively small volume. Beuther et al. (2007), Kauffmann et al. (2010), and Svoboda et al. (2016) have suggested schemes to study the physical conditions required in the Galactic SF regions to form HM stars. Particularly, Kauffmann et al. (2010) (hereafter, K10) found that Galactic low-mass SF regions satisfy the relation  $M \leq 870 M_{\odot} \left[ \frac{R}{\text{pc}} \right]$ , where  $0.01 < \left[ \frac{R}{\text{pc}} \right] < 10$ . Kauffmann & Pillai (2010) studied the HM SF Orion region (Hillenbrand 1997), and established the presence of massive stars in clouds more massive than that given by the above relation. For practical purposes, in the present work we redefine the K10 relation as

$$\left[ \frac{M}{M_{\odot}} \right] \geq 870 \left[ \frac{R_{\text{eff}}}{\text{pc}} \right]^{1.33}. \quad (3)$$

In rest of this paper, we will refer this mass–size threshold criterion to form HM stars as K10 relation, in reference Kauffmann et al. (2010). These authors had also suggested a slightly steeper (index 1.7) relation for a smaller range of sizes ( $1 < \left[ \frac{R}{\text{pc}} \right] < 4$ ). Considering that our sample covers the full range of sizes, we use the K10 criterion with index 1.33 in this work.

The mass–size diagram for our IRDCs is shown in Figure 4. In this Figure, the K10 criterion is traced with the solid blue line and striped area, while the distribution of the masses of the IRDCs as a function of their  $R_{\text{eff}}$  is plotted with the black

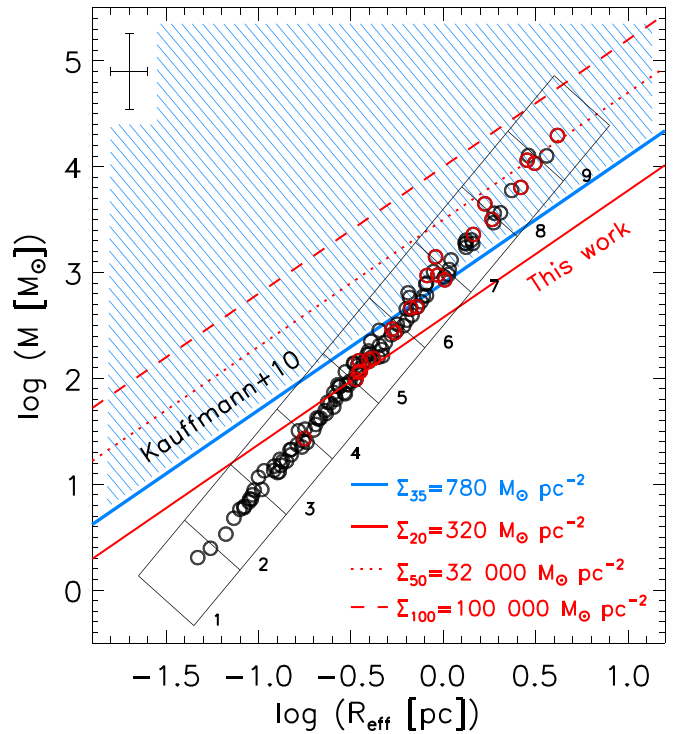


**Figure 5.** Bin distribution of the mass–size IRDC data. Details are the same as in Figure 4. The binning is done over the slanted distribution, as is shown with the numbered black boxes. The IRDCs with HLYSOs (defined in the text) are plotted with red circles, while the total IRDCs are shown with the black/red circles. A similar relation to K10 criterion for a threshold HMSF for the IRDCs in this work are plotted with the solid, dashed, and dotted red lines and are described in the text. The mean error of the data is shown in the upper left region of the diagram.

circles. The masses and effective radii of the IRDCs were obtained as described in Section 3. A fit was performed on these data, resulting in a power-law relation of the form  $M = \Sigma_0 \pi R_{\text{eff}}^2$ . In this relation, the constant  $\Sigma_0$  has a value  $\sim 300 M_{\odot} \text{pc}^{-2}$ , consistent with the median surface density value of the IRDCs sample.

In R17, we have tabulated masses of all YSOs embedded in our sample of IRDCs. In that study, YSOs classified as high luminosity YSO (HLYSOs; bolometric luminosities  $L_{\text{bol}} > 10 L_{\odot}$ ) are candidates for HM YSOs. Typically,  $L_{\text{bol}} = 10 L_{\odot}$  corresponds to a star of  $1.5 M_{\odot}$  if it is Class I YSO, or  $2 M_{\odot}$  if it is Class II YSO. Given that YSOs in these early phases are still accreting, they are likely to end up as HM stars.

The availability of masses allows us to analyze the mass–radius relation for our sample of IRDCs. We started our analysis by identifying IRDCs that contain at least one HLYSO. These IRDCs are marked in red circles in Figure 5. Clearly, there is a tendency for massive-large IRDCs to contain a HLYSO, as against lower values of mass–size of IRDCs. However, not all IRDCs satisfying the K10 criterion harbor a HLYSO. To understand the behavior in more detail, we analyze the fraction of IRDCs containing at least one HLYSO in small intervals of mass and radius along the mass–radius relation followed by our IRDCs. These intervals are shown as boxes in Figure 5. We characterize each box by the mean mass of IRDCs in that box. In Figure 6, we plot the fraction of IRDCs containing at least one HLYSO as a function of the mean mass for each bin (red line connecting circles). In the plot, we also show the fraction of IRDCs that contain at least

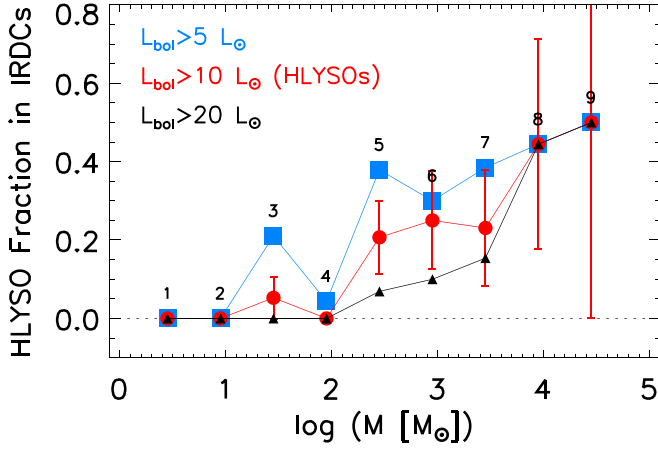


**Figure 6.** HLYSO fraction in IRDCs for each bin defined in Figure 5 as function of masses of the IRDCs, for three ranges of luminosities as is labeled in the top left region.

one YSO of  $L_{\text{bol}} > 5 L_{\odot}$  (blue line connecting squares) and  $L_{\text{bol}} > 20 L_{\odot}$  (black line connecting triangles). The fraction of IRDCs containing high luminosity YSOs clearly increases with increasing IRDC mass. The frequency of finding HM YSOs in IRDCs of our sample that satisfy the K10 criterion is 26% for  $\sim 500 M_{\odot}$ , which increases monotonically to  $\sim 50\%$  for the most massive IRDCs (from  $10,000 M_{\odot}$  to  $20,000 M_{\odot}$ ).

IRDCs that satisfy the K10 criterion are usually considered as sites of massive star formation. Twenty-six percent of our IRDCs satisfy the K10 criterion, but only one-third of these contain massive YSOs. This suggests that not all IRDCs are currently forming massive stars. We further find that more massive an IRDC is, it has a higher probability of forming a massive star. In our sample, the probability is unity only for the IRDCs with mass  $> 10^4 M_{\odot}$ . The statistics of the presence or not of massive YSOs in our sample of IRDCs allows us to generalize the K10 mass–size relation, by replacing the “constant” in Equation (3) by  $\Sigma_p$ :

$$\left[ \frac{M}{M_{\odot}} \right] \geq \Sigma_p \left[ \frac{R_{\text{eff}}}{\text{pc}} \right]^{1.33}, \quad (4)$$

where  $\Sigma_p$  is the threshold surface gas density of IRDCs that have percentage probability,  $p$ , of finding a massive YSO. We find that the K10 criterion refers to  $p = 35$  or  $\Sigma_{35} = 870 M_{\odot} \text{pc}^{-2}$ . Our IRDCs have  $\Sigma_{20} = 320 M_{\odot} \text{pc}^{-2}$ ,  $\Sigma_{50} = 32,000 M_{\odot} \text{pc}^{-2}$ .

#### 4.2. Star Formation Efficiency in the IRDCs

The star formation activity in the IRDC sample can be measured through the star formation efficiency (SFE) and the star formation law. For IRDCs, the SFE is obtained using the simple expression,  $\text{SFE} = M_{\text{star}} / (M_{\text{star}} + M_{\text{IRDC}})$ , where  $M_{\text{star}}$  is the “stellar” mass obtained by adding the masses of the YSOs embedded in each IRDC, and  $M_{\text{IRDC}}$  is the mass of the IRDC, obtained in Section 3. The masses of the YSOs were obtained from the R17 study. The SFE distribution (in percentage) for the IRDCs is shown in Figure 7 (solid histogram).

The IRDCs have SFE values between 0.01% and 30% with a median value of  $\sim 1\%$  (vertical dashed line), whereas the SFE values for IRDCs with HLYSOs (plotted with a dashed line histogram) range from 0.5% to 16%, with a similar median

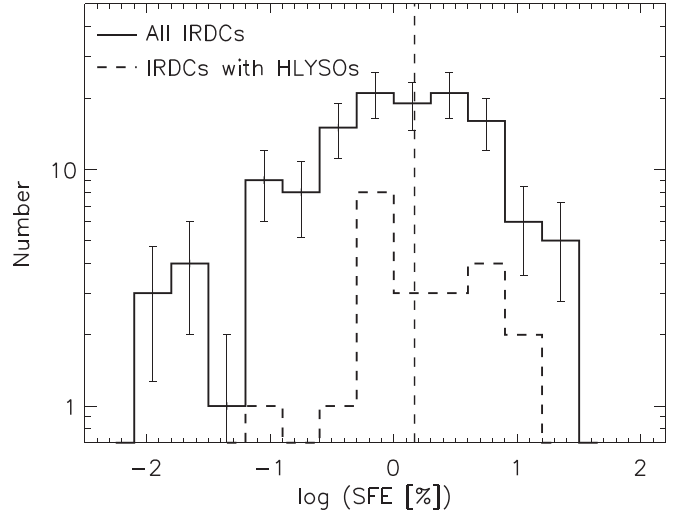


**Figure 7.** SFE Histograms of our IRDC sample. The solid line shows SFE for our entire sample of 129 objects, whereas the dashed line shows the histogram for the IRDCs containing HLYSOs. The vertical line shows the median value  $\sim 1\%$  for the entire sample. The error bars correspond to the statistical uncertainties in each bin ( $\sqrt{N}$ ).

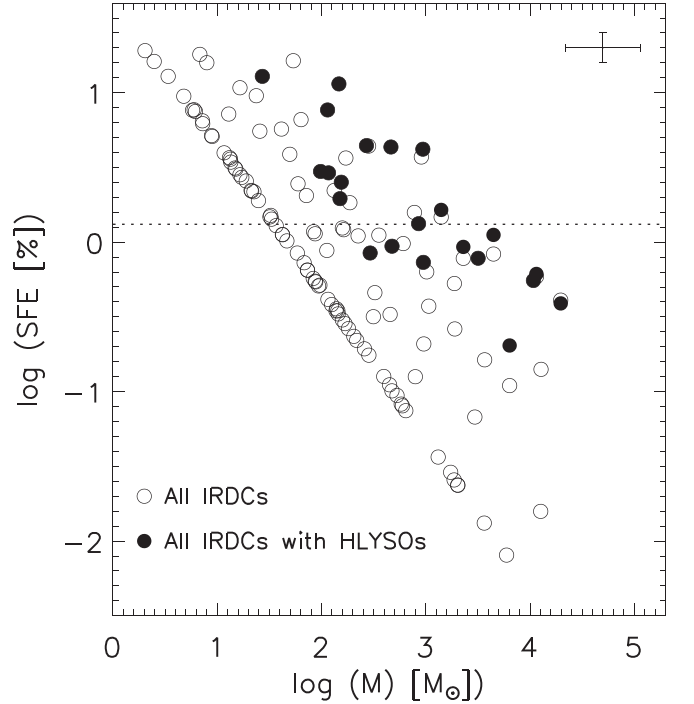


**Figure 8.** SFE–Mass distribution of the IRDCs. The open circles show all IRDCs data, while the filled circles show the position of the IRDCs with HLYSOs associated. The dashed line mark the median value of SFE for all IRDCs,  $\sim 1\%$ . The mean error of the data is shown in the right-upper region of the diagram.

value as for the entire population. Thus, to form an intermediate to HM star, the SFE of the IRDC should be higher than 0.5%. Below this efficiency, IRDCs do not form HLYSOs.

Figure 8 shows the SFE as a function of IRDC mass. In this figure, the IRDCs harboring massive stars are distinguished (solid circles) from the rest (open circles). Above  $100 M_{\odot}$ , IRDCs containing massive stars are the most efficient in every mass range. At the same time, there is a systematic decrease in SFE as the cloud mass increases. Given the mass–radius

relation (Figure 4), massive clouds are also larger. Hence, the most efficient HM SF IRDCs are the most compact ones ( $R_{\text{eff}} < 1$  pc), whose mass happens to be  $< 1000 M_{\odot}$  in IRDC samples.

#### 4.3. IRDCs and the Formation of Star Clusters

The definition of star cluster varies widely and depends on our limited knowledge to trace their members and their projected spatial distribution. From the literature, some definitions have physical motivation, while others are based on their data features. Lada & Lada (2003) define a star cluster as groups  $\geq 35$  YSOs with YSO surface densities ( $\Sigma_{\text{YSO}}$ ) of  $\geq 3$  YSOs  $\text{pc}^{-2}$ . On other hand, Carpenter (2000), using Ks band surface density maps, identified clusters as regions with overdensities with  $\sim 32$  YSOs  $\text{pc}^{-2}$ . Megeath et al. (2012) and Allen et al. (2007) used a similar criterion, but with a threshold overdensity defined as  $\sim 10$  YSOs  $\text{pc}^{-2}$ .

Our IRDC sample has surface densities ranging from 0.1 to  $\sim 100$  YSOs  $\text{pc}^{-2}$ , with a median value of 6 YSOs  $\text{pc}^{-2}$  and one outlier of 160 YSOs  $\text{pc}^{-2}$ . Around 40% of our IRDCs can be considered as hosts of star clusters if we adopt 10 YSOs  $\text{pc}^{-2}$  as the threshold surface density. If the IRDCs with HLYSOs are only considered, the surface density values vary from 0.1 to 40 YSOs  $\text{pc}^{-2}$ , with a median of 2 YSOs  $\text{pc}^{-2}$ , which curiously is lower than for our total IRDC sample. This trend can be explained as follows. IRDCs with HLYSOs have areas greater than  $0.3 \text{ pc}^2$  (median value), as can seen in Figure 3 (right). These large clouds generally have longer distances. High  $\Sigma_{\text{YSO}}$  values in these may be due to high numbers of HL and LLYSOs detected. Lower  $\Sigma_{\text{YSO}}$  values may be due to few LLYSOs detected, as expected for clouds with far distances. For all IRDCs in the sample, the range of  $\Sigma_{\text{YSO}}$  is greater and the median is higher, given the increment of the detection of YSOs in nearby clouds; additionally, it is possible to detect smaller IRDCs, achieving a most complete census of their stellar population.

Additionally, our IRDCs have a  $\Sigma_{\text{gas}}$  ranging from 200 to  $400 M_{\odot} \text{ pc}^{-2}$ , equivalent to  $0.04\text{--}0.08 \text{ g cm}^{-2}$ , with a mean value of  $0.07 \text{ g cm}^{-2}$ . These values are one order of magnitude lower than HM threshold density given by Krumholz & McKee (2008) of  $1 \text{ g cm}^{-2}$ , but similar to values found by Kainulainen & Tan (2013) in IRDCs and Rathborne et al. (2009) for Galactic HMSF regions. Thus, our IRDCs could be considered potential sites to form star clusters.

#### 4.4. Star Formation Law in the IRDCs

To study the surface density of the star formation rate ( $\Sigma_{\text{SFR}}$ ) distribution as a function of gas-surface density ( $\Sigma_{\text{gas}}$ ) in the IRDCs, first we obtained the  $\Sigma_{\text{SFR}}$  using the stellar mass ( $M_{\text{star}}$ ) of the YSOs embedded in the IRDC. The area used to compute the  $\Sigma_{\text{SFR}}$  is obtained in Section 3. The  $\Sigma_{\text{SFR}}$  and  $\Sigma_{\text{gas}}$  values for the IRDCs are shown in the Figure 9. In this figure, the open circles show all IRDCs, with those containing HLYSOs indicated by red circles. The IRDCs without YSO detection are plotted with the down-arrow symbols in the diagram. Our sample of IRDCs occupies a very small range of surface gas densities around a median  $\Sigma_{\text{gas}} \sim 319 M_{\odot} \text{ pc}^{-2}$  (vertical dashed line). Roughly, 92% of the IRDCs have  $\Sigma_{\text{gas}}$  values between  $250 M_{\odot} \text{ pc}^{-2}$  and  $400 M_{\odot} \text{ pc}^{-2}$  (vertical dotted lines). However, in this small range of  $\Sigma_{\text{gas}}$ , the  $\Sigma_{\text{SFR}}$  values range over four orders of magnitudes ( $\sim 10^{-2} M_{\odot} \text{ Myr}^{-1} \text{ pc}^{-2}$ – $10^2 M_{\odot} \text{ Myr}^{-1} \text{ pc}^{-2}$ ).

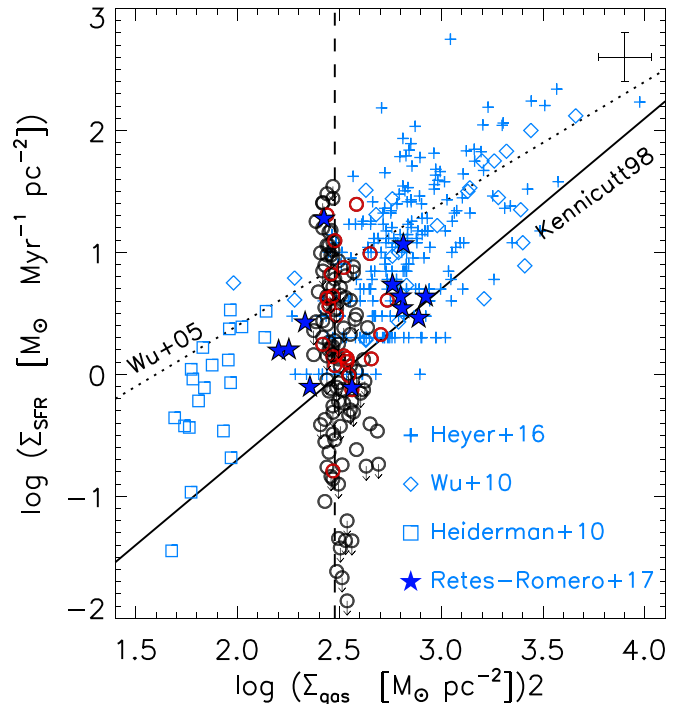


**Figure 9.**  $\Sigma_{\text{SFR}}$  distribution as function of  $\Sigma_{\text{gas}}$  for the IRDCs. The data for all IRDCs are plotted with open black/red circles, while the IRDCs with HLYSOs are plotted with open red circles, respectively, as in Figure 5. The extragalactic relations for this diagram are plotted with the solid line for the Kennicutt (1998) and the dotted line for Wu et al. (2005) relations. Data from Galactic massive clumps are plotted in blue diamonds and crosses, and the Galactic nearby LMSF regions are plotted with blue squares (See details in the text). The Galactic HMSF MC data from R17 are plotted in solid blue stars. The mean error of the IRDC data is shown in the upper right region.

The lack of any  $\Sigma_{\text{gas}}\text{--}\Sigma_{\text{SFR}}$  relation is in direct contrast with the well-known relation for SF clouds/galaxies established by Wu et al. (2005, dotted line), and Kennicutt (1998, solid line).

The large spread in  $\Sigma_{\text{SFR}}$  is likely due to the following reasons. Those IRDCs with  $\Sigma_{\text{SFR}}$  above the Wu et al. (2005) relation are likely to contain dense gas at small scales that are above the saturation limit at  $8 \mu\text{m}$ . Thus, the determined  $\Sigma_{\text{gas}}$  for these IRDCs is highly underestimated. On the other hand, IRDCs with  $\Sigma_{\text{SFR}}$  below the Kennicutt (1998) relation could be far IRDCs with few locations having the gas-surface density above the threshold density for star formation, as has been suggested in the literature (Heiderman et al. 2010; Retes-Romero et al. 2017). Additionally, these IRDCs may be in early star formation phase, associated with lower  $\Sigma_{\text{SFR}}$  values from 0.02 to  $5.0 M_{\odot} \text{ Myr}^{-1} \text{ pc}^{-2}$ , or/and their low-mass YSO population are not detected due to their large distances  $> 3$  kpc (ranging from 3.4 to 5.4 kpc).

Figure 9 also shows the global  $\Sigma_{\text{gas}}$  and  $\Sigma_{\text{SFR}}$  values for the MCs that harbor our sample of IRDCs, taken from R17. MCs cover a large range in  $\Sigma_{\text{gas}}$ , but a smaller range of  $\Sigma_{\text{SFR}}$ . In this figure, we also show the  $\Sigma_{\text{SFR}}\text{--}\Sigma_{\text{gas}}$  distribution for Galactic SF clumps. Almost all of the clumps currently forming massive stars from Heier et al. (2016) and Wu et al. (2010) are denser than our IRDCs. However, our higher  $\Sigma_{\text{SFR}}$  values are similar to the values for these clumps. Compared with nearby SF MCs of Heiderman et al. (2010), our IRDCs have higher  $\Sigma_{\text{gas}}$  values by a factor of four, but with similar mean values of  $\Sigma_{\text{SFR}}$ .

One of the characteristics of IRDCs is their small dynamic range in  $\Sigma_{\text{gas}}$ . This is likely to arising from the following two

effects. The first one is observational, derived from obtaining  $\tau_8$  using Spitzer 8  $\mu\text{m}$  data for the IRDCs. The use of the Galactic MIR background light to obtain  $\tau_8$  is sensitive only for a small range of gas densities, then an agglomeration of  $\Sigma_{\text{gas}}$  values in a narrow dynamic range is expected, as was discussed earlier in Section 3. The second reason is related to an intrinsic property. The fact that  $\Sigma_{\text{gas}}$  values to be clustered at  $\sim 300 M_{\odot} \text{pc}^{-2}$  may be due to the presence of an underlying mass–size relation  $M \propto L^2$ , where  $L$  is the maximum linear dimension of the cloud, first proposed for MCs by Larson (1981), and more recently revised by Lada et al. (2013). Indeed, the mass–size relation described in S4.1 give us a  $M \propto R_{\text{eff}}^2$  relation for the IRDCs with a proportionality constant to be  $\Sigma_0 = 300 M_{\odot} \text{pc}^{-2}$ . Taking into account the above, both can originate the narrowing of the  $\Sigma_{\text{gas}}$  range; however, the observational bias in the selection of the IRDCs is the most probable cause to produce the clustering of  $\Sigma_{\text{gas}}$ .

## 5. Conclusions

In this work, we studied the properties of IRDCs with and without massive YSOs, and the relation between these properties and HM star formation. The IRDCs were searched in MCs harboring embedded HM star formation activity. Physical and star formation properties of the IRDCs are explored, focusing in the mass–size relation, HMSF threshold, and the star formation law. The main conclusions are summarized. In total, we have found 835 YSOs in 128 IRDCs. From these, 108 YSOs are of intermediate to HM, representing the 13% of the stellar content embedded in the IRDCs.

1. Our sample of IRDCs have mean surface densities of  $319 M_{\odot} \text{pc}^{-2}$ , a mean mass of  $1062 M_{\odot}$ , and a mass function power law with index  $-1.8$ , which are similar to the corresponding properties for the full sample of IRDCs. The index for the mass function is comparable to other studies in IRDCs and Galactic clumps with HM star formation.
2. We find that a 33% of the IRDC sample contain at least one intermediate to massive YSO and satisfy the often-used mass–size criterion to forming massive stars. However, not all IRDCs satisfying the mass–size criterion contain massive stars. While that using the presence of HMYSOs in the IRDCs, its setting up a 20% probability for a mass–size relation containing HM young stars.
3. We find a clear tendency for more massive IRDCs to have a higher probability of containing a massive YSO. Twenty-five (20%) of our IRDCs are potential sites to harbor stellar clusters with masses higher than  $100 M_{\odot}$ .
4. Our sample of IRDCs do not show a relation for the star formation law. This is understandable given the narrow range of gas-surface densities of IRDCs.

This work was supported by the INAOE research fellowship “Beca de Colaboración” granted to R.R. We acknowledge comments and suggestions from the anonymous referee that led

to refinements in our work and improved the overall presentation of the paper.

## ORCID iDs

R. Retes-Romero  <https://orcid.org/0000-0002-1626-9229>  
Y. D. Mayya  <https://orcid.org/0000-0002-4677-0516>

## References

- Allen, L., Megeath, S. T., Gutermuth, R., et al. 2007, in *Protostars and Planets V*, 951 ed. B. Reipurth, D. Jewitt, & K. Keil (Tucson, AZ: Univ. of Arizona Press), 361
- Alves, J., Lombardi, M., & Lada, C. J. 2007, *A&A*, 462, 17
- André, P., Men’shchikov, A., & Bontemps, S. 2010, *A&A*, 518, 102
- Bastian, N., Covey, K. R., & Meyer, M. R. 2010, *ARA&A*, 48, 339
- Beuther, H., Churchwell, E. B., McKee, C. F., et al. 2007, in *Protostars and Planets V*, ed. B. Reipurth, D. Jewitt, & K. Keil (Tucson, AZ: Univ. Arizona Press), 165
- Beuther, H., & Steinacker, J. 2007, *ApJ*, 656, 85
- Bronfman, L., Nyman, L., & May, J. 1996, *A&AS*, 115, 81
- Butler, M. J., & Tan, J. C. 2012, *ApJ*, 754, 5
- Carpenter, J. M. 2000, *AJ*, 120, 3139
- Clemens, D. P. 1985, *ApJ*, 295, 422
- Egan, M. P., Shipman, R. F., Price, S. D., et al. 1998, *ApJ*, 494, 199
- Evans, N. J., II, Dunham, M. M., Jorgensen, J. K., et al. 2009, *ApJS*, 181, 321
- Faúndez, S., Bronfman, L., Garay, G., et al. 2004, *A&A*, 426, 97
- Gomez Gonzalez, L. 2012, PhD thesis, Univ. of Bonn
- Hartmann, L. W., & Kenyon, S. J. 1996, *ARA&A*, 34, 207
- Heiderman, A., Evans, N. J., II, Allen, L. E., et al. 2010, *ApJ*, 723, 1019
- Henshaw, J. D., Caselli, P., Fontani, F., et al. 2014, *MNRAS*, 440, 2860
- Heyer, M., Gutermuth, R., Urquhart, J. S., et al. 2016, *A&A*, 588, 29
- Hillenbrand, L. A. 1997, *AJ*, 113, 1733
- Jackson, J. M., Rathborne, J. M., Shah, R. Y., et al. 2006, *ApJ*, 163, 145
- Kainulainen, J., & Tan, J. C. 2013, *A&A*, 549, 53
- Kauffmann, J., & Pillai, T. 2010, *ApJ*, 723, 7
- Kauffmann, J., Pillai, T., Shetty, R., et al. 2010, *ApJ*, 716, 433
- Kennicutt, R. C. 1998, *ApJ*, 498, 541
- Könyves, V., André, P., Men’shchikov, A., et al. 2010, *A&A*, 518, 106
- Kramer, C., Stutzki, J., Rohrig, R., & Corneliussen, U. 1998, *A&A*, 329, 249
- Krumholz, M. R., & McKee, C. F. 2008, *Natur*, 451, 1082
- Lada, C. J., & Lada, E. A. 2003, *ARA&A*, 41, 57
- Lada, C. J., Lombardi, M., Román-Zúñiga, C., Forbrich, J., & Alves, J. F. 2013, *ApJ*, 778, 133
- Larson, R. B. 1981, *MNRAS*, 194, 809
- Megeath, S. T., Gutermuth, R., Muzerolle, J., et al. 2012, *AJ*, 144, 192
- Ossenkopft, V., & Henning, Th. 1994, *A&A*, 291, 943
- Perault, M., Omont, A., Simon, G., et al. 1996, *A&A*, 315, L165
- Peretto, N., & Fuller, G. A. 2009, *A&A*, 505, 405
- Peretto, N., & Fuller, G. A. 2010, *ApJ*, 723, 555
- Ragan, S. E., Bergin, E. A., & Gutermuth, R. A. 2009, *ApJ*, 698, 324
- Ragan, S. E., Henning, T., & Beuther, H. 2013, *A&A*, 559, 79
- Rathborne, J. M., Jackson, J. M., & Simon, R. 2006, *ApJ*, 641, 389
- Rathborne, J. M., Jackson, J. M., Simon, R., et al. 2009, *Ap&SS*, 324, 155
- Retes-Romero, R., Mayya, Y. D., Luna, A., & Carrasco, L. 2017, *ApJ*, 839, 113
- Roman-Duval, J., Jackson, J. M., Heyer, M., et al. 2009, *ApJ*, 699, 1153
- Schisano, E., Rygl, K. L. J., Molinari, S., et al. 2014, *ApJ*, 791, 27
- Simon, R., Jackson, J. M., Clemens, D. P., Bania, T. M., & Heyer, M. H. 2001, *ApJ*, 551, 747
- Simon, R., Rathborne, J. M., Shah, R. Y., et al. 2006, *ApJ*, 653, 1325
- Svoboda, B. E., Shirley, Y. L., Battersby, C., et al. 2016, *ApJ*, 822, 59
- Tognelli, P., Prada Moroni, P. G., & Degl’Innocenti, S. 2011, *A&A*, 533, 109
- Wang, K., Zhang, Q., Testi, L., et al. 2014, *MNRAS*, 439, 3275
- Willis, S., Guzman, A., Marengo, M., et al. 2015, *ApJ*, 809, 87
- Wu, J., Evans, N. J., II, Gao, Y., et al. 2005, *ApJL*, 635, L173
- Wu, J., Evans, N. J., II, Shirley, Y. L., et al. 2010, *ApJS*, 188, 313